

High-throughput Parasitic-independent Probe Thermal Resistance Calibration for Robust Thermal Mapping with Scanning Thermal Microscopy

Ram Munde,¹ Heng-Ray Chuang,¹ and Raisul Islam^{*1,2}

¹⁾*Department of Materials Engineering, Purdue University, West Lafayette, USA*

²⁾*Elmore Family School of Electrical and Computer Engineering, Purdue University, West Lafayette, IN USA*

(*Electronic mail: raisul@purdue.edu)

(Dated: 28 January 2026)

Nanostructured materials, critical for thermal management in semiconductor devices, exhibit a strong size dependence in thermal transport. Studying thermal resistance variation across grain boundaries is critical for designing effective thermal interface materials. Frequency-domain Thermoreflectance (FDTR)-based techniques can provide thermal resistance mapping at the micrometer (μm) scale. Scanning Thermal Microscopy (SThM) enables quantification of local thermal transport with significantly higher spatial resolution ($< 100 \text{ nm}$). However, challenges in quantifying the raw signal to thermal conductivity and surface sensitivity limit its widespread adoption for understanding nanoscale heat transport and defect-mediated thermal properties in nanostructured films. Here, we introduce a circuit-based probe thermal resistance (R_p) calibration technique independent of parasitic heat pathways, enabling accurate determination of probe heat dissipation and tip temperature rise, thereby allowing extraction of local thermal resistance. SThM achieved sub-100 nm spatial resolution in mapping thermal resistance across a 15 nm-thick Al film deposited via e-beam evaporation on SiO_2 substrate. The thermal resistance maps are converted to thermal conductivity using robust analytical and finite element models that account for tip-sample geometry, lateral heat spreading, and buried interface effects. Gaussian distribution fitting of pixel-level thermal resistance values yields $k_{\text{Al}} = 45.1_{-3.6}^{+4.7} \text{ W/(m}\cdot\text{K)}$ for the ultra-thin Al film (13–15 nm), representing a 5.3-fold reduction from bulk aluminum (237 W/(m·K)). These results agree with published experimental data and theoretical frameworks explaining thickness-dependent heat transport in ultra-thin metallic films.

I. INTRODUCTION

Across the last two decades, continuous materials scaling coupled with precise nanostructuring has powered a remarkable run of progress in electronic^{1–3}, photonic^{4,5}, and quantum technologies⁶, reinforced by advances in MEMS/NEMS^{7,8}, nanoscale sensors for biomedicine^{9–11}, and scanning-probe/optical instrumentation¹². Miniaturization fundamentally modifies transport, mechanical, and interfacial behavior. As a result, size-dependent variations in material properties become critical considerations in modeling, metrology, and device design. For example, silicon (Si) thermal conductivity (k) is reduced from its bulk k value of 138 W/m·K to 2.2 W/m·K for a 155 nm Si thin film^{13,14}. When the physical dimension becomes comparable to or smaller than the mean free path (Λ) of heat carriers (electrons and phonons), the macroscopic equilibrium and continuum assumptions break down. Therefore, understanding the nanoscale energy transport phenomena, both analytically and experimentally, is crucial for the continued miniaturization of technology.

Thermal metrology plays a vital role in validating theoretical models and advancing the understanding of energy transport mechanisms. Conventional techniques such as μ -thermocouples, microbridge and suspended devices (3ω), infrared thermography (IR), and liquid crystal thermography are used to measure macroscopic thermal properties of devices. Recently, with technological advancements in device

fabrication and deposition processes, the 3ω technique has been extended for use with thin films and microscale devices by fabricating bridges a few μm thick¹⁵. This method enables accurate characterization of both in-plane and cross-plane thermal transport in metallic, semiconducting, and dielectric thin films. A major limitation of the 3ω technique is its requirement for complex sample preparation and the complexities arising from voltage oscillations when measuring metals and semiconductors, thus limiting its applicability to a narrow range of materials¹⁶. Optical based techniques such as frequency- and time-domain thermoreflectance spectroscopy (FDTR and TDTR), Raman spectroscopy, laser flash techniques, and fluorescence techniques are widely used for measuring the temperature and thermal transport properties of microstructured materials^{17–19}. In contrast to the 3ω method, optical-based techniques such as TDTR and FDTR enable non-contact characterization of thermal properties, minimizing physical interference with the sample. Recent advancements in laser source technology have significantly enhanced the capability of TDTR and FDTR techniques to characterize the thermal properties of materials with superior temporal and spatial resolution²⁰. Depending on the type of laser used in the measurement, these methods can achieve temporal resolutions ranging from a few nanoseconds to $\sim 30 \text{ fs}$ ($1 \text{ fs} = 10^{-15} \text{ sec}$). It is worth noting that the electronic relaxation time (τ_e) typically lies in the range of about ~ 10 –50 fs. Therefore, TDTR and FDTR are useful techniques for measuring the thermal transport properties associated with electron-phonon coupling mechanisms. However, these optical-based thermal measurement methods suffer from an intrinsic spatial resolu-

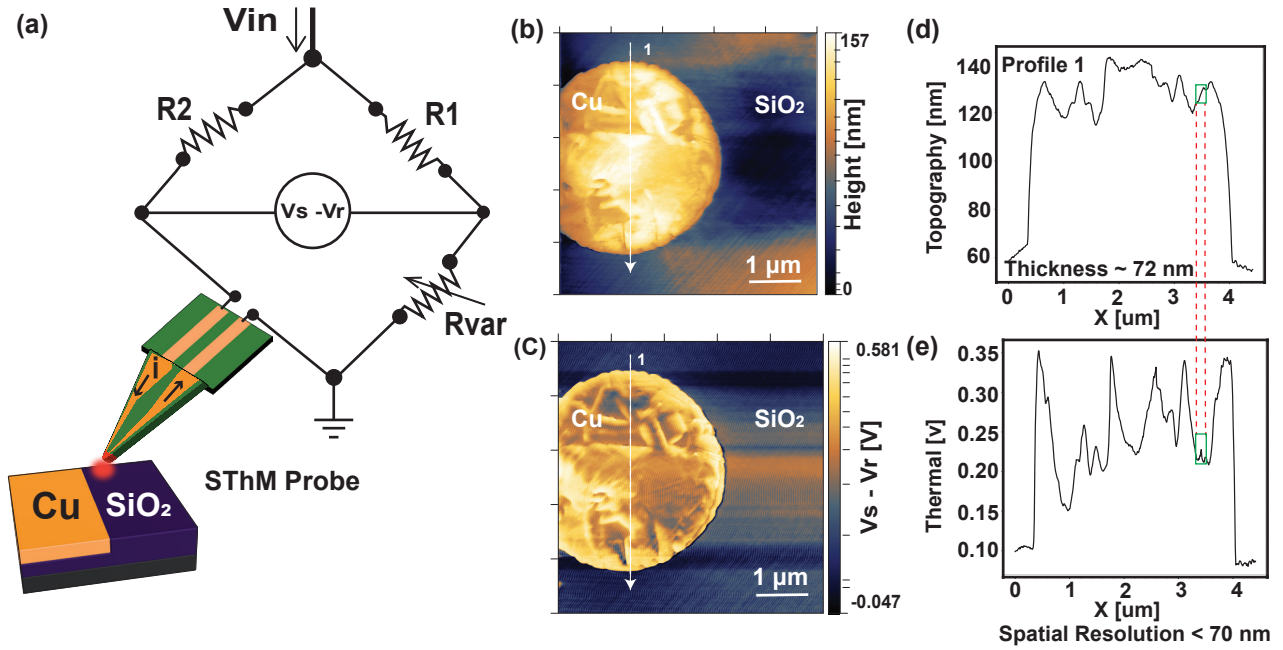


FIG. 1. (a) Schematic of a Kelvin Nanotechnology (KNT) thermistor probe with an integrated Wheatstone bridge for high-precision thermal signal detection. The input voltage (V_{in}) supplied using integrated software, while variable resistor balances the bridge by matching tip resistance at the equilibrium conditions. (b) SThM topography and (c) SThM thermal signal maps of a $5 \mu\text{m} \times 5 \mu\text{m}$ Cu-Through Silicon Via (TSV) sample. The thermal signal in (c) reveals local thermal conductivity contrast arising from grain boundary and surface roughness variation. (d) SThM topography [nm] signals and (e) SThM thermal signal [V] profiles along line 1. Consecutive changes in thermal signal peaks, with no corresponding change in topography, demonstrate that the spatial resolution of local thermal conductivity mapping is $< 70 \text{ nm}$.

tion limitation imposed by the pump-probe spot size (typically $\sim 0.5\text{--}10 \mu\text{m}$), rendering them inadequate for reliably imaging thermal heterogeneities arising from nanoscale defects.

In the late 1990s, the development of scanning probe microscopy (SPM)-based techniques, such as scanning thermal microscopy (SThM) and near-field scanning optical microscopy (NSOM) provided unprecedented spatial resolution for nanoscale characterization and manipulation. In general, NSOM requires optically compatible and flat samples, is limited by weak signal-to-noise ratio, and exhibits greater tip fragility compared to SThM. Table I summarizes the quantitative capabilities of thermal metrology techniques for microelectronics. Current commercially available SThMs are based on the working principle designed by Majumdar *et al.*²¹ as illustrated in Fig. 1(a). The SThM system uses specialized thermal probes (TPs) with tip radii below 100 nm, capable of resolving temperature differences smaller than $0.1 \text{ }^\circ\text{C}$ with sub-100 nm spatial resolution, thereby enabling quantitative nanoscale thermal characterization of materials. SThM can operate in either temperature contrast mode (TCM) or conductivity contrast mode (CCM). In TCM, a tip-integrated thermocouple measures the junction temperature at the tip-sample interface, whereas the CCM mode provides qualitative mapping of local thermal conductivity across a broad range of materials, including metallic, semiconducting, and dielectric thin films. Transforming these qualitative signals into quantitative thermal conductivity values is not trivial because

of the complex coupled thermal transport at the tip-sample interface. There is no standardized technique for obtaining quantitative measurements of thermal resistance with SThM. Recently, various theoretical modeling, calibration strategies, and instrument add-on techniques have been reported^{22–24}. Bodzenta *et al.* and Li *et al.* provided comprehensive reviews of SThM theoretical models and experimental strategies for quantitative thermal measurements^{24,25}.

In this work, we present a circuit-based calibration technique for measuring non-contact thermal resistance (R_{nc}), also known as probe thermal resistance. Compared with conventional thermal-stage methods, this calibration approach reduces sensitivity to temperature-controller errors and environmental factors (e.g., moisture), and is less affected by common artifacts, including calibration-sample variations. First, we construct thermal-resistance maps across the film surface by coupling scanning thermal measurements with finite-element heat-transfer modeling of the tip-sample mechanical contact. These maps resolve spatial variations in thermal transport that arise from differences in crystallite size and orientation, effects that are most pronounced in polycrystalline and amorphous films. Because the maps carry the imprint of surface preparation and condition—the same steps a film undergoes in routine device-integration flows—the resulting resistance estimates reflect the as-processed device film. Building on the same calibrated contact model, we then extract the film's effective thermal conductivity (k_{eff}) using an experimentally anchored procedure that combines accurate instrument cali-

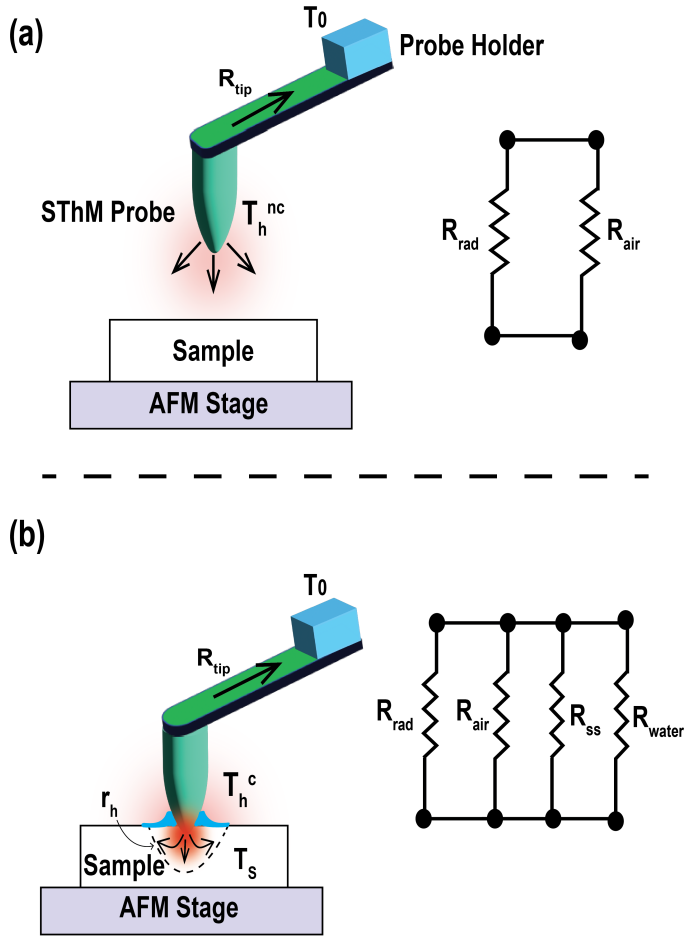


FIG. 2. (a) Heat transfer pathways of the probe just before sample contact. The thermal resistances shown include: R_{tip} (heat dissipation at the tip), R_{rad} (radiative thermal resistance), and R_{air} (convective thermal resistance). (b) Heat transfer pathways when the probe is in contact with the sample, introducing additional thermal resistance channels through the solid-solid (R_{ss}) contact which includes R_{tip} and R_{water} is the conduction due to water meniscus forming at tip-sample contact.

bration with contact heat-transfer modeling. Sec. II of this paper discusses the theoretical modeling of SThM required for understanding different heat transfer mechanisms at the tip-sample contact. Sec. III describes the methodology used to extract k_{eff} of samples and the post-processing steps to study the underlying nanoscale thermal transport physics and to map the corresponding thermal resistances. In Sec. IV, we present the results obtained through the techniques described in Secs. II and III. Finally, we summarize our results with concluding remarks.

II. BACKGROUND OF THE QUANTITATIVE STHM MEASUREMENT TECHNIQUE

A schematic of the SThM probe with an integrated Wheatstone bridge is shown in Fig. 1(a). The Wheatstone

bridge helps detect changes in the thermal resistance of the temperature-sensitive tip material. SThM provides qualitative maps of both the thermal signal and the surface topography of the scanned region, as shown in Fig. 1(b,c). The topography map reveals the nanoscale geometrical features of the surface, whereas the thermal signal maps offer qualitative insights into the local thermal conductivity of the sample with nanoscale spatial resolution. Furthermore, SThM exhibits a high signal-to-noise ratio, enabling more accurate and reliable measurements (see Fig. 1(d,e)). However, correlating these measured signals with the intrinsic thermal properties of the materials requires a thorough theoretical understanding of the underlying physical mechanisms.

Theoretical modeling links the probe voltage signals measured by the Wheatstone bridge detector to the sample's thermal properties. Therefore, accurate quantitative measurements of thermal conductivity heavily rely on mathematical modeling to transform probe voltage signals into thermal conductivity values. Thermal transport between the probe and sample involves multiple heat transfer channels, including conduction through the solid-solid contact (tip-sample) and the water meniscus (from the moisture), convection through air, and thermal radiation, which becomes significant at nanometer scale tip-sample distances (see Fig. 2). Each of these channels has its corresponding contribution, which depends on the instrumentation, measurement environment, and sample under consideration. Various analytical and numerical approaches have been reported for studying each heat transfer channel and its significance in quantitative measurements. A recent review by Li *et al.* comprehensively discusses multiple analytical and numerical approaches for calculating heat transfer through these channels²⁴.

This work uses a thermistor probe tip that consists of Palladium (Pd) resistor material with a thermal coefficient of resistance (TCR) of 3800 ppm/°C, as specified by the manufacturer. Importantly, the TCR value is not affected by the experimental procedure or daily use of the probe^{27,28}. Since Pd is a metal, within a relatively small temperature range, the electrical resistance of the tip (Ω) varies linearly with temperature (T).

$$\Omega = \Omega_o \left[1 + \alpha(\tilde{T} - T_0) \right] \quad (1)$$

where Ω_o is the electrical resistance of the tip at temperature T_0 and α is the TCR. The tip temperature is measured by applying an electric current to the probe and monitoring the change in electrical resistance of the tip with SThM software.

When the probe is in air without contacting the sample, heat is dissipated by conduction through the cantilever, convection through the air, and radiation to the ambient, as shown in Fig. 2(a). The heat transport is governed by Fourier's law of conduction, as presented in Eq. (2). The steep tip-sample temperature gradient may challenge the applicability of Fourier's law. However, when the mean free path (Λ) of the dominant heat carriers is much smaller than the tip radius (~ 50 nm), and the SThM operates at slow scan rates (0.5–1 Hz, corresponding to > 1 ms per pixel), local thermal equilibrium is maintained^{29,30}. Therefore, Fourier's

TABLE I. Thermal Metrology Techniques for Microelectronics

Technique	Mechanism	Spatial Resolution	Temperature Resolution
Infrared thermography	Thermal radiation (Planck, Stefan–Boltzmann)	3–10 μm	0.02–1 K
Photothermal Raman	Raman shift or Stokes/anti-Stokes ratio	0.5–1 μm	1–10 K
3ω method	AC Joule heating with electrical sensing	—	0.1 mK–1 K
TDTR / FDTR	Reflectivity-based transient thermometry	1–10 μm	~0.01 K
NSOM	Near-field optical heat detection	50–100 nm	0.1–1 K
SThM	AFM-integrated thermocouple/Pd thermistor tip	10–50 nm	~0.1 K

Data adapted from Refs.^{15,17,26}.

law with an effective thermal conductivity can still be applied as a simple analytical model of heat transport. When the tip contacts the sample, a solid–solid tip–sample junction introduces an additional heat-conduction pathway, as described by Eq. (3). Based on the heat-transfer channels illustrated in Fig. 2(a,b), the relationships between the thermal resistances in non-contact and contact configurations are given by Eqs. (4) and (5), respectively.

$$Q_h = \frac{\tilde{T}_h^{nc} - T_0}{R_{nc}} \quad (2)$$

$$Q_h = \frac{\tilde{T}_h^c - T_0}{R_{nc}} + \frac{\tilde{T}_h^c - T_s}{R_c} \quad (3)$$

$$\frac{1}{R_{nc}} = \frac{1}{R_{rad}} + \frac{1}{R_{air}} + \frac{1}{R_{tip}} \quad (4)$$

$$\frac{1}{R_c} = \frac{1}{R_{rad}} + \frac{1}{R_{air}} + \frac{1}{R_{ss}} + \frac{1}{R_{water}} \quad (5)$$

The current applied to the probe through the integrated SThM power controller induces Joule heating in both the

probe and the tip material. The probe current in CCM is higher than that in TCM. Under the constant-current condition of CCM, the generated electrical heat (Q_h) flows from the tip into the sample. Therefore, the amount of heat transfer depends on the thermal conductivity of the sample. For highly thermally conductive materials, heat dissipates rapidly, resulting in a small temperature rise at the tip and a correspondingly low output voltage. In contrast, materials with high thermal resistance impede heat flow, causing heat to accumulate near the tip and producing a larger temperature rise and higher voltage output. The corresponding temperature change (ΔT) can be expressed as shown in Eq. (6). Experimental verification of this relation is provided in Fig. S3 (Supplementary Material).

$$\Delta T = aV \quad (6)$$

Using Eq. (6), the thermal signals can be converted into the corresponding tip temperature as follows:

$$\Delta T^{nc} = \tilde{T}_h^{nc} - T_0 = aV^{nc} \quad (7)$$

$$\Delta T^c = \tilde{T}_h^c - T_0 = aV^c \quad (8)$$

Therefore, by substituting Eqs. (7) and (8) into Eqs. (2) and (3), we can obtain the relationship between the probe voltage and probe thermal resistance, as shown in Eq. (9):

$$\frac{\Delta T^{nc} - \Delta T^c}{\Delta T^{nc}} = \frac{V^{nc} - V^c}{V^{nc}} = \frac{\tilde{T}_h^{nc} - \tilde{T}_h^c}{\tilde{T}_h^{nc} - T_0} = \frac{1}{R_{nc} + R_c} \left(R_{nc} + \frac{T_0 - T_s}{Q_h} \right) \quad (9)$$

Furthermore, since the tip radius (b) is very small, the associated thermal radius (r_h) is negligible relative to the sample size ($>10 \text{ mm}^2$). Thus, under thermal equilibrium³¹, it is reasonable to approximate $T_0 \approx T_s$. Consequently, we obtain the following expression:

$$\frac{V^{nc} - V^c}{V^{nc}} = \frac{R_{nc}}{R_{nc} + R_c} \quad (10)$$

Therefore, using Eq. (10), the values of R_c and R_{nc} can be expressed in terms of the measured thermal signals (V^c and V^{nc}).

Here, R_c embodies the sample's thermal transport characteristics, and its detailed formulation will be discussed in Sec. III.

III. METHODS

A. Sample preparation

A 5 mm × 10 mm Al film is patterned on a SiO₂/Si substrate. A 6-inch CZ-prime wafer with a 1.5 μm SiO₂ film on its surface was diced into 12 mm × 12 mm pieces. The p-type (B doped) resistivity of the substrate is between 10-25 Ω-cm. The surface was first cleaned by sequentially sonicating in toluene, acetone, and 2-propanol for 5 minutes, then rinsed with DI water. During the process, non-polar and polar contaminants were cleaned with toluene and acetone, respectively, and 2-propanol was used to remove acetone from the substrate. A positive photoresist (AZ1518) was spin-coated at 3000 rpm for 60 s with a dwell time of 5 s, which was then followed by a soft bake at 110 °C for 60 s. The substrate was exposed using a Heidelberg MLA150 maskless aligner, with the laser set to 405 nm and a dose of 160 mJcm⁻². The sample was then developed in MF-26A for 35 s to remove the exposed photoresist over an area of 5 mm × 10 mm. A 15 nm Al film was evaporated by CHA e-beam evaporator. The evaporation was controlled by a Telemark 861 deposition controller, and the deposition rate was 2 Ås⁻¹. A lift-off step was applied to remove the photoresist and Al from the unexposed area, leaving a 5 mm × 10 mm Al film on the surface.

B. Experimental setup and numerical data generation

The thermal signal data are obtained from the experiments conducted using an AFM (Dimension Icon® manufactured by Bruker Inc.) equipped with an integrated SThM module. The SThM probe is purchased from Bruker Corp. and it consists of a thin Pd line on Si₃N₄ cantilever, as shown in Fig. S5 (Supplementary Material). This probe is pre-mounted on the probe holder, and the probe tip serves as one of the arms of the Wheatstone bridge, as shown in the schematic in Fig. 1(a). Before each SThM scan, the Wheatstone bridge is balanced to minimize background thermal signal noise. Subsequently, an input voltage (> 0.5 V) is applied to the probe. The temperature increase at the SThM tip changes the resistance of the Pd heater, producing a voltage imbalance across the Wheatstone bridge. This imbalance is detected as the SThM voltage signal ($V_s - V_r$). All measurements were conducted at a constant contact setpoint force and scan rate to ensure consistency. We used a gain of 1000× while extracting the change in voltage of the Pd heater. This gain helps amplify the corresponding thermal signals without any loss of information.

For thermal relaxation and steady-state measurements, the SThM tip rasters at a relatively low scan rate of 0.5–1 Hz (S2 supplementary material). This scan rate is maintained throughout the experiment to reduce variance in thermal signals due to thermal drift. The acquired images are analyzed using Gwyddion software, while the pixel-wise thermal signal data are extracted and processed through a specially developed Python code tailored for this study.

C. Measuring probe thermal resistance (R_{nc})

Understanding the heat transfer between the probe and the surrounding system is essential for the quantitative measurement of thermal conductivity. The probe dissipates a finite amount of heat into the surrounding environment even in the non-contact state. Accurate quantification of this background signal is necessary to isolate the intrinsic thermal contribution from the sample. In earlier reports, the measurement of non-contact thermal resistance (R_{nc}) was carried out by balancing the tip temperature using a thermal stage^{28,29}. This method, however, is prone to inaccuracies arising from parasitic thermal losses due to the roughness of the stage, non-uniform temperature profiles, and additional convective heat transfer to the probe.

We propose a circuit-based technique to measure the non-contact thermal resistance (R_{nc}) by monitoring the probe-tip Joule heating power and the resulting temperature rise under an applied voltage. Unlike stage-based techniques, this approach eliminates dependence on thermal stage sensitivity and minimizes the influence of parasitic thermal effects from the environment. In this approach, Joule heating from the applied current raises the tip temperature. The temperature rise is directly proportional to the input power, where the proportionality constant corresponds to the non-contact thermal resistance, R_{nc} (Eq.12). The temperature rise (ΔT) was calculated relative to the initial tip temperature, which was at room temperature ($T_0 \sim 294$ K), and the corresponding initial electrical resistance of the tip ($\Omega_0 \sim 177$ Ω). It is important to note that the probe electrical resistance (Ω_p), which is output of balanced Wheatstone bridge, differs from the tip resistance (Ω) due to the presence of built-in limiting resistors in the probe, as shown in Fig. S4 (Supplementary Material). The applied power (P_{tip}) was determined directly from Joule heating in the tip under the applied current using Eq.(11). The resulting data were fitted using linear regression, yielding an R_{nc} value of $(5.97 \pm 0.40) \times 10^4$ K/W as shown in Fig. 3. An instrumental uncertainty of ± 0.1 K in ΔT due to laser illumination was considered in the analysis³². It should be noted that the uncertainty associated with laser illumination may be relatively large; however, since the analysis focuses on the relative change in temperature (ΔT), the impact of this uncertainty is reduced. This result is consistent with previously reported values for similar probes, thereby validating the accuracy of the proposed measurement technique^{28,33}.

$$P_{tip} = \frac{V_{tip}^2}{\Omega(\tilde{T})} \quad (11)$$

$$R_{nc} = \frac{\Delta T}{P_{tip}} \quad (12)$$

Here, V_{tip} denotes the voltage drop across the tip, extracted from the known SThM probe resistance and the Wheatstone bridge input voltage (Fig. 1(a)).

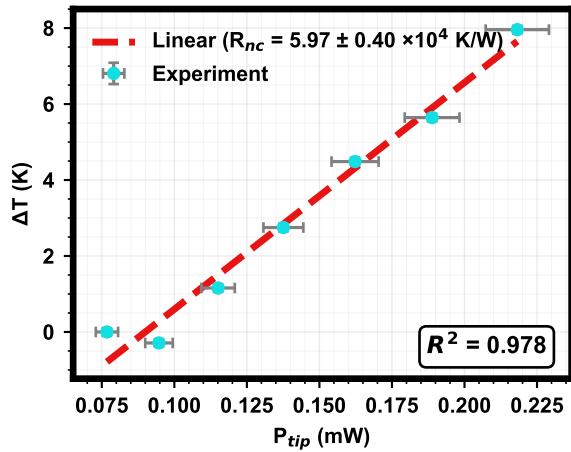


FIG. 3. SThM non-contact thermal resistance (R_{nc}) measured with monitored Joule heating.

D. Modeling contact thermal resistance (R_c)

As discussed in Sec. II, R_c is an experimentally measured quantity that comprises the thermal properties of the sample. In addition to solid-solid thermal resistance (R_{ss}), R_c also includes thermal resistances arising from radiation (R_{rad}), air conduction (R_{air}) and the water meniscus formed at the tip-sample contact (R_{water}). The contribution of radiative heat transfer is often considered negligible, particularly under ambient SThM conditions with a cantilever-sample separation larger than $1 \mu\text{m}$ ²⁴. The probe considered in our measurement has a tip height of $\sim 10 \mu\text{m}$ measured from the cantilever. In a humid environment, as shown in Fig. 2(b), a water meniscus forms at the tip-sample contact and serves as an additional pathway for heat transfer. A detailed study of water-meniscus formation and a theoretical model for heat transport through the meniscus were presented in Refs. 34 and 35, respectively. Furthermore, Refs. 36 and 37 reported that the contribution of the meniscus to the total tip-sample contact resistance (R_c) lies between 1% and 6%. Therefore, the water-meniscus effect is treated as a 6% uncertainty in the R_c values. Therefore, under the assumption that $R_{nc} \approx R_{tip}$, we express the measured quantity $(R_c - R_{nc})_{meas}$ as the sum of three thermal resistances, as shown in Eq. (13).

$$(R_c - R_{nc})_{meas} \approx R_{ss} = R_{int} + R_{spr} + f \cdot R_{BD} \quad (13)$$

where:

- R_{int} : Tip-sample interface thermal resistance
- R_{spr} : Spreading resistance (Yovanovich Eq. (14))^{38,39}
- $R_{BD} = 1/(h_{BD} \cdot \pi b^2)$: Interface boundary resistance
- $f = [b/(b + L_{spread})]^2$: Geometric dilution factor
- L_{spread} : Lateral spreading length

The impact of the interfacial thermal resistance (R_{int}) and its physically reasonable range are determined using FEM modeling, as discussed in Sec. IV. Furthermore, heat-spreading analysis is crucial for determining the thermal conductivity (k) of the sample. Yovanovich *et al.*^{38,40} and Muzychka *et al.*³⁹ derived analytical solutions for the thermal spreading resistance (R_{spr}), as shown in Eq. (14), for a film on a substrate as a function of the film thickness (t) and the thermal conductivities of the film (k_{eff}) and substrate (k_{sub}).

$$R_{spr} = \frac{1}{\pi k_{eff} b} \int_0^{\infty} \left[\frac{1 + K \exp(-2\xi t/b)}{1 - K \exp(-2\xi t/b)} \right] J_1(\xi) \sin(\xi) \frac{d\xi}{\xi^2} \quad (14)$$

where K is defined as $K = \frac{1 - k_{sub}/k_{eff}}{1 + k_{sub}/k_{eff}}$, b is the source radius, and J_1 is the first-order Bessel function of the first kind.

The buried interface thermal boundary conductance h_{BD} is a critical parameter in this analysis. However, as heat transfers through a thin film to the substrate, it spreads laterally before reaching the buried interface. The characteristic lateral spreading length (L_{spread}) determines the effective area over which heat crosses the buried interface. For heat flow from a localized source of radius b at the top of a thin film of thickness t and thermal conductivity k_{film} , deposited on a substrate with thermal conductivity k_{sub} , this spreading length is given by Eq. (15)⁴¹⁻⁴³.

$$L_{spread} = t \cdot \sqrt{\frac{k_{film}}{k_{sub}}} \quad (15)$$

This lateral spreading reduces the effective contribution of the buried interface resistance through a geometric dilution effect. The dilution factor f represents the fraction of interface resistance “seen” by the heat flux and is given by Eq. (16).

$$f = \left(\frac{b}{b + L_{spread}} \right)^2 = \left(\frac{b}{b + t \sqrt{k_{film}/k_{sub}}} \right)^2 \quad (16)$$

Physically, heat spreading reduces the effective contribution of interface resistance by the ratio of the original contact area to the expanded area at the interface. As the spreading length increases relative to the contact radius, more heat bypasses the localized interface resistance, thereby reducing its impact on the total thermal resistance.

A critical insight is that both $R_{spr}(k)$ and f depend on k_{film} , which is the unknown quantity we seek to determine. This creates a self-consistency requirement: the spreading resistance $R_{spr}(k)$ and the effective buried interface resistance $f(k) \cdot R_{BD}$ are both functions of the unknown film thermal conductivity. Consequently, the thermal resistance balance (Eq. 17)

$$R_{spr}(k) + f(k) \cdot R_{BD} = (R_c - R_{nc})_{meas} - R_{int} \quad (17)$$

must be solved iteratively to extract k_{film} . This iterative solution converges to yield the thermal conductivity of the thin film, with the complete algorithm detailed in the section S2. (Supplementary Material).

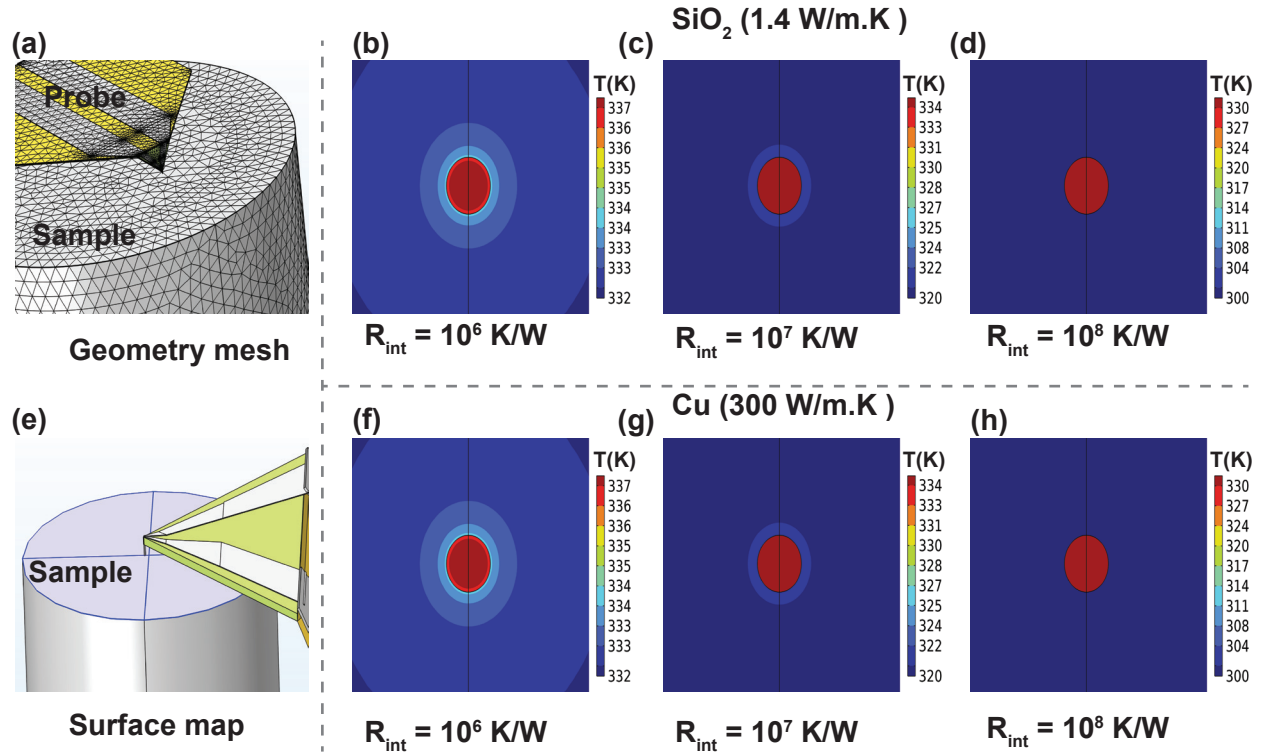


FIG. 4. (a) Custom meshed geometry of the SThM probe and the sample. The probe consists of a Si_3N_4 cantilever with Au connection pads and a Pd tip resistor. A 5 nm Ni–Cr thin layer is deposited between the Au pads and the Pd tip to suppress reverse heat transfer and to avoid sudden increases in Joule heating. (b) Effect of $R_{int} = 10^6 \text{ K/W}$ on the surface temperature of the SiO_2 sample and the SThM tip contact. (c) Temperature variation at the contact interface for $R_{int} = 10^7 \text{ K/W}$. (d) Reduced surface heating due to the higher thermal resistance of $R_{int} = 10^8 \text{ K/W}$. (e) Schematic representation of the sample surface in contact with the SThM tip. (f–h) Effect of R_{int} on the Cu surface for 10^6 , 10^7 , and 10^8 K/W , respectively.

IV. RESULTS AND DISCUSSION

A. Finite-element multiphysics modeling of SThM probe

The variation in the working environment of SThM measurements and the uncertainty in the thermal resistance of the tip-sample interface (R_{int}) make quantitative measurements challenging. Therefore, a fundamental understanding of thermal transport at the tip-sample interface is essential for the quantitative determination of local thermal conductivities of the sample. In this study, a detailed three-dimensional finite element model (3D-FEM) is developed to evaluate the interfacial thermal resistance (R_{int}) by simulating the heat transfer mechanisms occurring at the probe–sample junction. Accurate determination of R_{int} provides insights into the complex heat transfer pathways occurring between the tip and the sample. This 3D-FEM model is developed using COMSOL Multiphysics® to systematically explore the effects of multiple physical parameters on the tip–sample thermal interaction. Fig. 4(a) illustrates the SThM probe and sample structure, along with their meshed geometry. The probe comprises a Si_3N_4 cantilever, an Au pad connected to the tip, and a Pd

tip. Detailed dimensions and structural specifications of probe are provided in Fig. S5 (Supplementary Material). The model incorporates two primary physical processes: (1) heat transfer in solids and (2) electromagnetic heating (Joule heating in the Pd resistor). All exposed surfaces are set as adiabatic, except for the interface between the tip and the sample.

The quasi-equilibrium heat transfer equation with internal Joule heating is employed to model heat transport throughout the system:

$$-\nabla \cdot (\kappa \nabla T) = Q_e \quad (18)$$

where κ is the thermal conductivity. The volumetric Joule heat source Q_e arises from electrical biasing of the Pd thermistor and is given by

$$Q_e = \frac{V_p^2}{\Omega(T) \mathcal{V}_h} \quad (19)$$

Where V_p is the applied voltage, $\Omega(T)$ is the temperature-dependent electrical resistance of the Pd thermistor, and \mathcal{V}_h is the effective heater volume. This expression corresponds to uniform distribution of electrical power dissipation within the resistive element. Convection term was not considered in

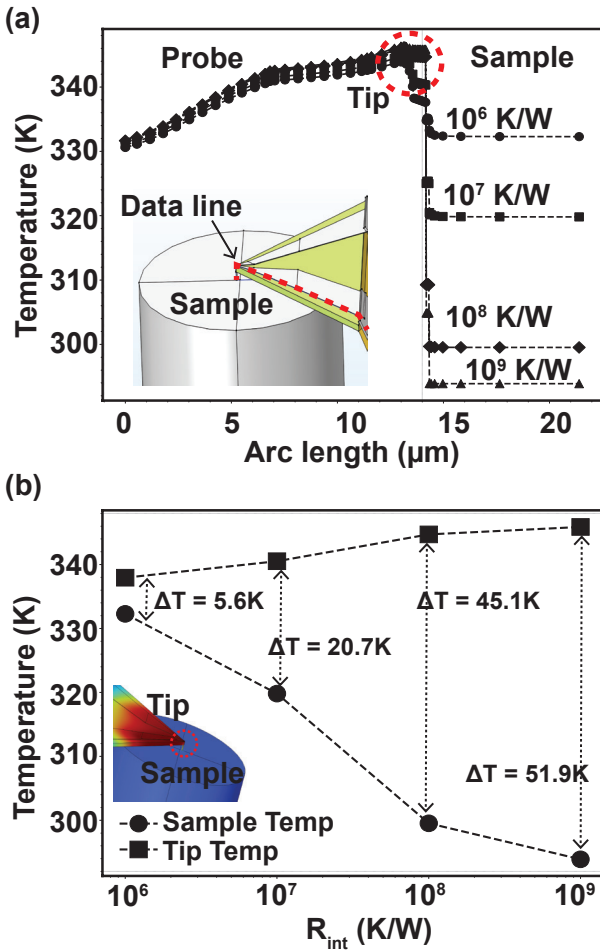


FIG. 5. (a) Temperature distribution along the arc length of data line for different thermal interface resistances (R_{int}). Data points are downsampled for clarity, with distinct markers and dotted lines highlighting the temperature trends for each R_{int} value. (b) Temperature difference ($\Delta T = T_{tip} - T_{sample}$) versus R_{int} , illustrating the monotonic increase of thermal decoupling with higher contact resistance. Together, these plots highlight the influence of R_{int} on probe–sample thermal coupling in SThM measurements.

Eqs. (18) due to its negligible contribution under the given experimental conditions^{25,29,44}.

The heat generated at the probe tip is transferred through the tip–sample interface and subsequently into the sample. To accurately capture the variation in R_{int} , the SThM tip–sample contact is modeled over a wide range of R_{int} values, from 10^6 to 10^9 K/W, as illustrated in Fig. 5(a). This simulation range is selected based on experimentally obtained thermal resistance values for nanoscale contacts^{24,45}. At low interfacial resistance ($R_{int} < 10^6$ K/W), the contribution of R_{int} to the overall thermal resistance (R_c) is negligible, indicating perfect heat transfer across the interface. On the other hand, at high interfacial resistance ($R_{int} > 10^9$ K/W), heat transfer between the tip and sample becomes significantly suppressed, effectively isolating the thermal transport pathways. The resulting probe temperature profiles for different R_{int} values are pre-

sented in Fig. 5(a). At high interface thermal resistance values ($R_{int} \geq 10^8$ K/W), the sample temperature remains constant at room temperature, indicating the absence of local heating. Therefore, R_{int} cannot exceed 10^7 K/W, since local heating of the sample is needed for thermal resistance measurement.

The effect of the R_{int} on local sample heating was examined for two materials with strongly contrasting intrinsic thermal conductivities: Cu (300 W/m·K) and SiO₂ (1.38 W/m·K). As shown in Fig. 4(b–d) for SiO₂ and Fig. 4(f–h) for Cu, identical values of R_{int} result in qualitatively similar surface temperature distributions beneath the tip, despite the large difference in bulk thermal conductivity. Because the COMSOL model considers smooth surfaces for all domains, the resulting temperature profiles for Cu and SiO₂ are expected to be identical, which is in agreement with previous studies showing that R_{int} is independent of the underlying material in the absence of surface roughness effects^{24,27,46}. At lower interfacial thermal resistance ($R_{int} \leq 10^6$ K/W), efficient heat transfer from the probe leads to a broader thermal diffusion profile in both materials. In contrast, increasing $R_{int} \geq 10^7$ K/W strongly suppresses heat flow across the interface, resulting in negligible local surface heating for both Cu and SiO₂. Importantly, the experimentally measured total thermal resistance lies in the range $\leq 10^7$ K/W and is accompanied by clear local surface heating beneath the probe. Therefore, R_{int} must be $\leq 10^7$ K/W and cannot exceed the experimentally inferred thermal resistance.

Furthermore, the difference between the SThM tip temperature and the corresponding local sample temperature variation is plotted in Fig. 5(b). The change in tip and sample temperature (ΔT) is shown for various R_{int} values. The results shown in Fig. 5(a,b) demonstrate that R_{int} plays a dominant role in the quantitative determination of the sample’s local thermal conductivity. While R_{int} is treated parametrically in the FEM simulations to examine its influence on the measured temperature response, this approach is adopted to establish a physically constrained relationship between the experimentally accessible temperature contrast $\Delta T = T_{tip} - T_{sample}$ and R_{int} . By comparing the experimentally measured ΔT (Fig. 3) with the trends predicted by the FEM model shown in Fig. 5 (b), a plausible and bounded range of R_{int} is identified for the given probe–sample contact conditions.

B. Experimental determination of model parameters

To experimentally validate the quantitative SThM model, a 15 nm aluminum (Al) thin film deposited on a SiO₂ substrate was selected as the test sample. The film was patterned adjacent to the bare SiO₂ substrate, enabling direct comparison between regions of differing thermal conductivity under identical measurement conditions. The sample preparation and fabrication details are provided in the Sec. III (A). All SThM measurements were carried out at a controlled room temperature of about 294 K, monitored continuously by a temperature regulation system. The SThM probe was positioned near the Al/SiO₂ interface and brought into mechanical contact with the sample surface. This contact led to a sudden reduction

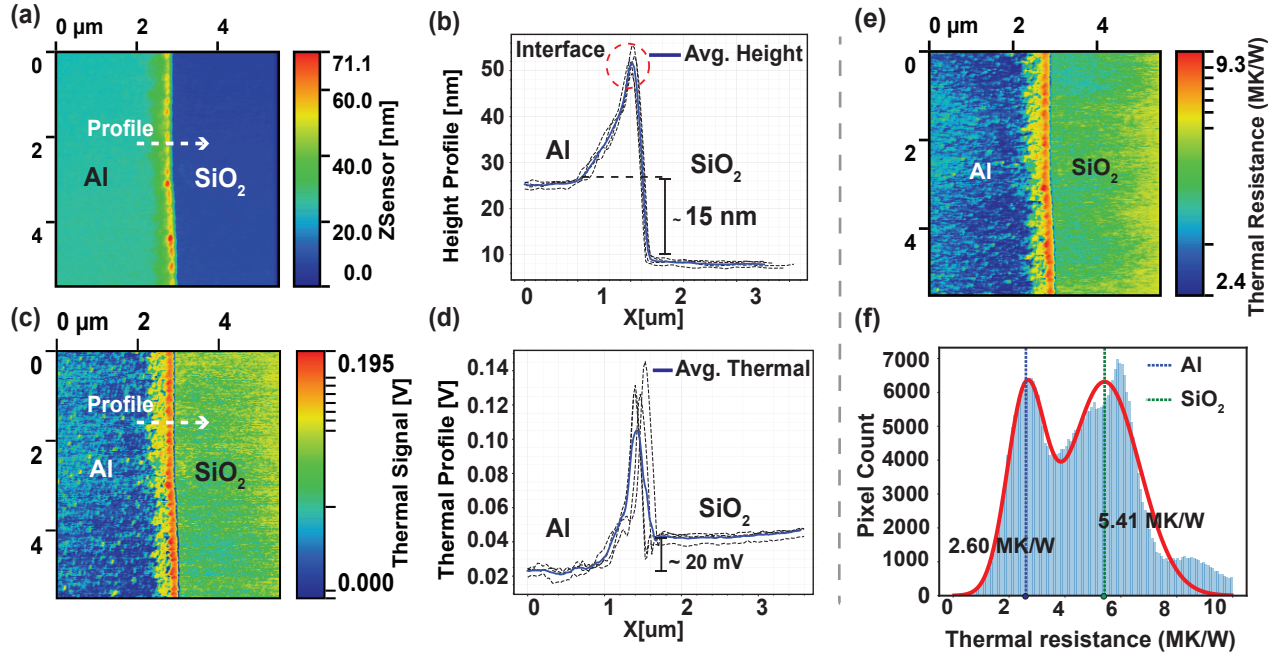


FIG. 6. (a) AFM topography image of a $5 \mu\text{m} \times 5 \mu\text{m}$ region of the Al/SiO₂ sample surface. (b) Corresponding height profile across the interface, showing a step height of 15 nm for the Al layer, consistent with the sample fabrication procedure. (c) SThM thermal signal map, where the lower heating voltage over Al indicates higher thermal conductivity compared to SiO₂. (d) Line profile of the thermal signal across the Al/SiO₂ interface, revealing elevated heating voltage at the boundary due to topography artifacts. A relative thermal signal difference of 20 mV is observed between Al and SiO₂ surfaces. (e) Thermal signal map converted to thermal resistance (R_c) map through calibrated mathematical modeling. (f) 1D histogram derived from pixel-to-pixel correlation of thermal signals, revealing prominent thermal resistances.

in probe temperature, indicating the activation of an additional thermal conduction pathway at the tip–sample junction, thereby enhancing heat dissipation into the sample (see Fig. S1 from the Supplementary Material). Subsequently, as the tip scanned the sample area, the probe recorded thermal signals from the sample as temperature variations, which allowed the calculation of the sample’s thermal resistance. A total of 7 independent SThM scans were acquired to ensure the reproducibility of the measurements. The corresponding pixel-level thermal signal and topography data were extracted using the SPM image analysis software named Gwyddion. The data were processed and analyzed using a custom-developed Python script designed specifically for quantitative pixel-wise thermal signal correlation and noise reduction. This in-house code enabled automated data extraction, normalization, and statistical comparison across multiple scans, significantly improving the accuracy and consistency of the thermal mapping results.

Figure. 6(a,c) shows the topography and thermal signal map of 15 nm-thick Al thin film patterned on a SiO₂ substrate. A strong thermal signal contrast was observed between the Al film and the SiO₂ substrate, reflecting the significant differences in their thermal conductivities. Two approach-retraction curves for either side of the interface are used for the conversion between the SThM signal and thermal resistance using Eq. (10). Further details about the approach-retraction curve are provided in Fig. S1 (Supplementary Material). The relative change in the thermal signal ($\sim 20 \text{ mV}$)

from the SiO₂ surface to the Al film corresponds to a decrease in thermal resistance from the SiO₂ surface to the 15 nm-thick Al film. Therefore, this decrease in thermal resistance indicates a higher thermal conductivity of the Al film compared to the SiO₂ substrate.

To extract the thermal resistance associated with Al and SiO₂, a pixel-to-pixel correlation between the height and thermal signal maps is performed. This correlation is used to construct a 2D histogram (see Fig. S2 from the Supplementary Material), which enables a separation of the thermal responses from Al and SiO₂ surfaces. Traditional analysis methods often rely on arbitrarily selected line-cuts or cropped regions of interest, introducing potential user bias in the selection process. In contrast, the present approach systematically processes all available data points from the thermal signals measurement, ensuring reproducibility and minimizing subjective interpretation. This comprehensive analysis leverages the full spatial information content, thereby improving statistical confidence in the extracted thermal properties. Subsequently, the acquired data are subjected to statistical processing to extract thermal properties. However, this analysis is susceptible to errors arising from experimental artifacts—such as surface contamination, tip–sample contact variations, or instrumental noise—which can distort the thermal signal and compromise measurement accuracy. Therefore, to quantitatively extract representative thermal resistance values while accounting for spatial heterogeneity, a 2D histogram of thermal resistance on the y-axis and film thickness on the x-

axis is constructed (Fig. S2 of Supplementary Material). This histogram is then projected onto the thermal resistance axis to obtain statistically representative values. This projection combines measurements across all thickness values, yielding a one-dimensional distribution from which statistically robust resistance values can be determined. The resulting 1D distribution is modeled using a double-Gaussian function, from which the mean peak positions corresponding to the thermal resistances of Al and SiO_2 are extracted. The statistical uncertainties in these mean values are obtained from the covariance matrix of the nonlinear least-squares fitting procedure. From this analysis, the mean thermal resistances were found to be $2.60 \pm 0.03 \text{ MK/W}$ and $5.41 \pm 0.04 \text{ MK/W}$ for Al and SiO_2 , respectively.

The measured thermal resistances $R_{\text{meas}}(\text{SiO}_2) = 5.41 \pm 0.04 \text{ MK/W}$ and $R_{\text{meas}}(\text{Al}) = 2.60 \pm 0.03 \text{ MK/W}$ provide the experimental foundation for quantitative determination of the thermal conductivity of the Al thin film. Following the theoretical framework established in Sec. III, we model the measured contact-to-noncontact thermal resistance difference as a series combination of three contributions: the tip-sample interfacial thermal resistance (R_{int}), the sample spreading resistance (R_{spr}), and the Al/ SiO_2 buried interface thermal boundary resistance (R_{BD}), as given by Eq. (13). This formulation enables direct extraction of the Al thermal conductivity from the experimental data through an iterative algorithm (Eq. 17) that accounts for the interdependence of R_{spr} and R_{BD} on the unknown film thermal conductivity.

1. Tip Interface Resistance R_{int} Extraction

As shown in Fig. 6(e), the experimentally measured $(R_c - R_{nc})_{\text{meas}}$ values are $\leq 10^7 \text{ K/W}$. Therefore, it can be concluded that R_{int} is also $\leq 10^7 \text{ K/W}$. In addition, the tip-sample contact resistance (R_{int}) is mainly governed by surface roughness, the applied tip-sample normal force, and the resulting contact area^{27,46,47}. Therefore, the thermal contact between the SThM probe and the sample may slightly differ for Al and SiO_2 surfaces; however, it is very challenging to determine the exact R_{int} for each case. Therefore, for simplification, we assumed the same R_{int} for both Al and SiO_2 interfaces. This assumption introduces negligible uncertainty in the measurement because both surfaces exhibit comparable roughness (see Fig. S6 in the Supplementary Material). Additionally, the tip-sample normal contact force was maintained with an AFM setpoint value of $\sim 0.6 \text{ V}$, which corresponds to $< 10 \text{ nN}$ contact force for this type of probes. Therefore, the tip-sample interface resistance R_{int} is extracted from a reference measurement on bare SiO_2/Si (no thin film, $R_{\text{BD}} \approx 0$).

$$R_{\text{int}} = R_{\text{meas}}(\text{SiO}_2) - R_{\text{spr}}(\text{SiO}_2/\text{Si}) \quad (20)$$

where $R_{\text{spr}}(\text{SiO}_2/\text{Si})$ is calculated using Eq. (14) with known k_{SiO_2} (1.38 W/m·K) and k_{Si} (150 W/m·K). The parameters used in this analysis are provided in Table S1 (supplementary material).

TABLE II. Thermal resistance budget breakdown.

Component	Value (MK/W)	Percentage	Description
R_{int} (tip-Al)	1.84	70.8%	Tip-sample interface
R_{spr} (Al/ SiO_2)	0.68	26.2%	Spreading resistance
$f \cdot R_{\text{BD}}$ (Al/ SiO_2)	0.08	3.1%	Diluted R_{BD}
Total	2.60	100%	$= R_{\text{meas}}$

2. Iterative Algorithm for k Extraction

Literature values for metal/dielectric interfaces^{48–51} span a considerable range. For the Al/ SiO_2 interface, we adopt a central value of $h_{\text{BD}} = 200 \text{ MW}/(\text{m}^2\text{K})$ with a realistic range of $h_{\text{BD}} = 150\text{--}250 \text{ MW}/(\text{m}^2\text{K})$ to account for this uncertainty^{52–54}.

Applying the iterative algorithm to the experimental measurements yields a thermal conductivity of $k_{\text{Al}} = 45.1 \text{ W}/(\text{m}\cdot\text{K})$ at the central values of $h_{\text{BD}} = 200 \text{ MW}/(\text{m}^2\text{K})$ and $t = 14 \text{ nm}$. See Section S3 (supplementary material) for the detailed calculation. In our 15 nm Al film, a sub-stoichiometric $\text{Al}_2\text{O}_{3-x}$ layer ($\sim 1\text{--}2 \text{ nm}$ thick) forms naturally on the Al surface due to exposure to ambient air^{55,56}, reducing the effective conductive metallic thickness to approximately 13–14 nm. A comprehensive uncertainty analysis accounting for variations in both interface conductance ($h_{\text{BD}} = 150\text{--}250 \text{ MW}/(\text{m}^2\text{K})$) and film thickness ($t = 13\text{--}15 \text{ nm}$) produces asymmetric error bounds of $+4.7\% / -3.6 \text{ W}/(\text{m}\cdot\text{K})$, yielding a final result of $k_{\text{Al}} = 45.1_{-3.6}^{+4.7} \text{ W}/(\text{m}\cdot\text{K})$. This represents a 5.3-fold reduction from bulk aluminum (237 W/m·K), consistent with Fuchs-Sondheimer theory^{57,58} for films of thickness comparable to the electron mean free path ($t/\lambda_e \approx 0.93$). The thermal resistance budget (Table II) reveals that the tip-sample interface dominates the total measured resistance (70.8%), with spreading resistance contributing 26.2% and the diluted buried interface resistance only 3.1%. The geometric dilution factor of $f = 0.148$ indicates that lateral heat spreading over a characteristic length of $L_{\text{spread}} \approx 80 \text{ nm}$ substantially reduces the effective contribution of the Al/ SiO_2 interface resistance. A complete matrix of extracted thermal conductivity values for all combinations of h_{BD} and thickness is provided in the Table S1 of Supplementary Material.

TABLE III. Phonon thermal conductivity (k_p), electron thermal conductivity (k_e), and total thermal conductivity (k) of bulk aluminum from literature

Metal	k_p (W/m·K)	k_e (W/m·K)	k (W/m·K)
Al	6	246	237–252

Data adapted from Refs.^{59,60}.

DISCUSSION

The thermal conductivity of Al consists of both phonon (k_p) and electron (k_e) contributions, with electrons typically dom-

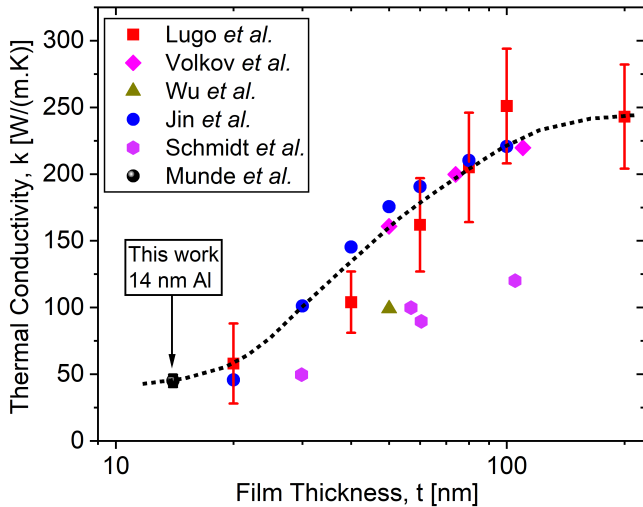


FIG. 7. Thickness-dependent thermal conductivity of polycrystalline Al thin films. The SThM result from this work (14 nm Al, $k = 45.1^{+4.7}_{-3.6}$ W/(m·K)) is benchmarked against reported values from Lugo *et al.*⁶¹, Volkov *et al.*⁶², Wu *et al.*⁶³, Jin *et al.*⁶⁴, and Schmidt *et al.*⁶⁵. The dashed curve is a trend line, consistent with the Fuchs-Sondheimer^{57,58} model incorporating Mayadas-Shatzkes⁶⁶ grain boundary scattering. Data spread reflects variations in film microstructure and measurement techniques.

inating heat transport in bulk. Jain *et al.* performed detailed first-principles calculations to examine both phonon-phonon and electron-phonon scattering processes in bulk Al, quantitatively determining the individual contributions of k_p and k_e to the overall thermal conductivity⁵⁹. Furthermore, they quantified the mean free path (Λ) distributions of both phonon and electron heat carriers by analyzing their respective thermal conductivity accumulation functions at 300 K (see Fig. S7 of Supplementary Material). Analysis of the thermal conductivity accumulation function demonstrates that the electron contribution decreases substantially as Λ decreases, indicating that electrons with short Λ contribute less to heat transport than those with longer Λ .

The accumulation function data at 300 K indicate that phonon thermal conductivity in Al is dominated by carriers with mean free paths ranging from 1 nm to 22 nm (comprising $\sim 90\%$ of k_p), while electron thermal conductivity requires longer mean free paths of 10 nm to 25 nm for similar accumulation ($\sim 90\%$ of k_e). The onset of contributions also differs markedly: phonon transport begins at $\Lambda \sim 1$ nm, whereas electron transport only becomes substantial at $\Lambda > 10$ nm. These characteristic length scales directly impact thermal transport in confined geometries. This confinement preferentially suppresses electron transport, as the film dimension is smaller than the typical electron mean free paths, resulting in diffuse boundary scattering that significantly reduces k_e .

Fig. 7 compares the SThM-extracted thermal conductivity of the 14 nm Al film ($k = 45.1^{+4.7}_{-3.6}$ W/(m·K)) with literature values for polycrystalline Al thin films of varying thickness measured by different techniques, including frequency-domain thermoreflectance (FDTR)⁶⁵, photothermal mirage⁶³,

electrical heating with temperature profile analysis⁶¹, and electron diffraction thermometry⁶². Boltzmann transport equation (BTE) modeling results from Jin *et al.*⁶⁴ are also included. Our result falls on the expected trend of decreasing thermal conductivity with decreasing film thickness, consistent with enhanced electron scattering at surfaces and grain boundaries.

The dashed curve in Fig. 7 is a trend line that captures the thickness-dependent behavior and remains consistent with the combined Fuchs-Sondheimer and Mayadas-Shatzkes electron scattering model^{57,58,66}. Using the literature value of $\lambda_e = 19$ nm for the electron mean free path in aluminum⁶⁷, this theoretical framework predicts $k = 49.5$ W/(m·K) for a 14 nm film (Supplementary Section S4), which falls within our experimental uncertainty range. The spread in literature data reflects variations in film microstructure, deposition conditions, and measurement techniques across different studies. The agreement between our SThM measurement, the theoretical prediction, and existing literature data validates the iterative extraction methodology developed in this work.

The thermal signal and topography appear elevated along the Al/SiO₂ boundary (see Fig. 6(a, c)). The elevated topography introduces a minor artifact in the thermal signal due to AFM feedback sensitivity effects at the step height. Consequently, the higher thermal resistance extracted at the edge arises from the same artifact, as it is directly derived from the thermal signal. Nevertheless, Fig. 6(e) demonstrates the significant potential of this approach for probing thermal transport variations across dislocation defects and grain boundaries with sub-100 nm spatial resolution. Furthermore, validation using established approaches, such as those described in Refs. 18 and 20 for assessing thermal property variations across grain boundaries with different densities, would be highly beneficial, particularly given the high spatial resolution offered by SThM.

V. CONCLUSION

We experimentally quantified the thermal resistance of the SThM probe using a circuit-based calibration method and employed FEM modeling to investigate the underlying heat transfer mechanisms. The contributions of various probe-sample heat transfer channels, along with their corresponding measurement strategies, were systematically examined. Furthermore, the thermal conductivity of a 15 nm Al thin film, deposited by e-beam evaporation on a few-micrometer-thick SiO₂ substrate, is measured. The robustness of the pixel-to-pixel correlation approach for extracting representative thermal signals is discussed. In addition, statistical and measurement uncertainties in thermal resistance are quantified, considering the underlying assumptions. The measured thermal conductivity of the Al thin film is in good agreement with the theoretical frameworks and the published experimental data.

Overall, as demonstrated in this study, the SThM-based thermal metrology approach enables quantitative and spatially resolved characterization of thermal transport at the

nanoscale. This technique provides sub-100 nm lateral resolution, allowing direct mapping of local heat conduction pathways with precision far beyond that achievable by conventional optical methods such as TDTR and FDTR. Unlike TDTR and FDTR, which are fundamentally constrained by optical diffraction limits and thermal penetration depth—thereby limiting their reliability for ultrathin films—SThM imposes no such thickness restrictions. This advantage makes it particularly effective for studying two-dimensional materials, nanoscale heterostructures, and complex interfaces. SThM emerges as a powerful and complementary tool for nanoscale thermal transport characterization, offering insights into defect-, boundary-, and interface-driven effects that are inaccessible through traditional macroscopic or optical approaches.

SUPPLEMENTARY MATERIAL

See the supplementary material for the raw data that supports the main findings of this study.

ACKNOWLEDGMENTS

We acknowledge Dr. Amy Marconnet, Professor of Mechanical Engineering at Purdue University, for her valuable guidance and for providing access to the COMSOL license.

DATA AVAILABILITY STATEMENT

The experimental and modeling data that support the findings of this study are available from the corresponding author upon reasonable request.

REFERENCES

- A. Kelleher, "Celebrating 75 years of the transistor a look at the evolution of moore's law innovation," in *2022 International Electron Devices Meeting (IEDM)* (2022) pp. 1.1.1–1.1.5.
- R. E. Munde, N. Vaillancourt, H.-R. Chuang, C. Gu, Y. Wang, and R. Islam, "3d integrated system for advanced intelligent computing," *Advances in Physics: X* **10**, 2599301 (2025).
- K. Banerjee, S. J. Souris, P. Kapur, and K. C. Saraswat, "3-d ics: A novel chip design for improving deep-submicrometer interconnect performance and systems-on-chip integration," *Proceedings of the IEEE* **89**, 602–633 (2002).
- O. Ostroverkhova, "Organic optoelectronic materials: mechanisms and applications," *Chemical reviews* **116**, 13279–13412 (2016).
- X. Huang, D. Ji, H. Fuchs, W. Hu, and T. Li, "Recent progress in organic phototransistors: Semiconductor materials, device structures and optoelectronic applications," *ChemPhotoChem* **4**, 9–38 (2020).
- D. S. C. Putranto, R. W. Wardhani, J. Ji, and H. Kim, "A deep inside quantum technology industry trends and future implications," *IEEE Access* (2024).
- J. Zhu, X. Liu, Q. Shi, T. He, Z. Sun, X. Guo, W. Liu, O. B. Sulaiman, B. Dong, and C. Lee, "Development trends and perspectives of future sensors and mems/nems," *Micromachines* **11**, 7 (2019).
- S. E. Lyshevski, *MEMS and NEMS: systems, devices, and structures* (CRC press, 2018).
- S. Hannah, E. Blair, and D. K. Corrigan, "Developments in microscale and nanoscale sensors for biomedical sensing," *Current Opinion in Electrochemistry* **23**, 7–15 (2020).
- J. Wang, G. Chen, H. Jiang, Z. Li, and X. Wang, "Advances in nano-scaled biosensors for biomedical applications," *Analyst* **138**, 4427–4435 (2013).
- F. J. Tovar-Lopez, "Recent progress in micro-and nanotechnology-enabled sensors for biomedical and environmental challenges," *Sensors* **23**, 5406 (2023).
- D. G. Cahill, W. K. Ford, K. E. Goodson, G. D. Mahan, A. Majumdar, H. J. Maris, R. Merlin, and S. R. Phillpot, "Nanoscale thermal transport," *Journal of applied physics* **93**, 793–818 (2003).
- A. McConnell and K. E. Goodson, "Thermal conduction in silicon micro- and nanostructures," *Annual review of heat transfer* **14** (2005).
- X. Huang, S. Gluchko, R. Anufriev, S. Volz, and M. Nomura, "Thermal conductivity reduction in a silicon thin film with nanocones," *ACS applied materials & interfaces* **11**, 34394–34398 (2019).
- D. G. Cahill and R. O. Pohl, "Thermal conductivity of amorphous solids above the plateau," *Physical review B* **35**, 4067 (1987).
- D. G. Cahill, K. Goodson, and A. Majumdar, "Thermometry and thermal transport in micro/nanoscale solid-state devices and structures," *J. Heat Transfer* **124**, 223–241 (2002).
- J. Christofferson, K. Maize, Y. Ezzahri, J. Shabani, X. Wang, and A. Shakouri, "Microscale and nanoscale thermal characterization techniques," (2008).
- A. Tiwari, K. Boussois, B. Nait-Ali, D. S. Smith, and P. Blanchart, "Anisotropic thermal conductivity of thin polycrystalline oxide samples," *AIP Advances* **3** (2013).
- Z.-C. Zeng, H. Wang, P. Johns, G. V. Hartland, and Z. D. Schultz, "Photothermal microscopy of coupled nanostructures and the impact of nanoscale heating in surface-enhanced raman spectroscopy," *The Journal of Physical Chemistry C* **121**, 11623–11631 (2017).
- E. Isotta, S. Jiang, G. Moller, A. Zevalkink, G. J. Snyder, and O. Balogun, "Microscale imaging of thermal conductivity suppression at grain boundaries," *Advanced Materials* **35**, 2302777 (2023).
- A. Majumdar, J. Carrejo, and J. Lai, "Thermal imaging using the atomic force microscope," *Applied Physics Letters* **62**, 2501–2503 (1993).
- F. Guemann, J. W. Pomeroy, and M. Kuball, "Scanning thermal microscopy for accurate nanoscale device thermography," *Nano Today* **39**, 101206 (2021).
- Y. Li, Y. Zhang, Y. Liu, H. Xie, and W. Yu, "A comprehensive review for micro/nanoscale thermal mapping technology based on scanning thermal microscopy," *Journal of Thermal Science* **31**, 976–1007 (2022).
- Y. Li, J. Wu, J. Luo, J. Wang, W. Yu, and B. Cao, "Quantitative measurements in scanning thermal microscopy: Theoretical models, calibration technique, and integrated instrument," *Journal of Applied Physics* **138** (2025).
- J. Bodzenta and A. Kaźmierczak-Bałata, "Scanning thermal microscopy and its applications for quantitative thermal measurements," *Journal of Applied Physics* **132** (2022).
- Z. M. Zhang, Z. M. Zhang, and Luby, *Nano/microscale heat transfer*, Vol. 410 (Springer, 2007).
- G. Pernot, A. Metjari, H. Chaynes, M. Weber, M. Isaiev, and D. Lacroix, "Frequency domain analysis of 3ω -scanning thermal microscope probe—application to tip/surface thermal interface measurements in vacuum environment," *Journal of Applied Physics* **129** (2021).
- Y. Huang, J. Spiece, T. Parker, A. Lee, Y. Gogotsi, and P. Gehring, "Violation of the wiedemann–franz law and ultralow thermal conductivity of ti3c2t x mxene ," *ACS nano* **18**, 32491–32497 (2024).
- S. Deshmukh, M. M. Rojo, E. Yalon, S. Vaziri, C. Koroglu, R. Islam, R. A. Iglesias, K. Saraswat, and E. Pop, "Direct measurement of nanoscale filamentary hot spots in resistive memory devices," *Science advances* **8**, eabk1514 (2022).
- T. Swoboda, X. Gao, C. M. Rosário, F. Hui, K. Zhu, Y. Yuan, S. Deshmukh, Ç. K"oroğlu, E. Pop, M. Lanza, *et al.*, "Spatially-resolved thermometry of filamentary nanoscale hot spots in tio2 resistive random access memories to address device variability," *ACS Applied Electronic Materials* **5**, 5025–5031 (2023).

³¹Y. Gu, X. Ruan, L. Han, D. Zhu, and X. Sun, "Imaging of thermal conductivity with sub-micrometer resolution using scanning thermal microscopy," *International journal of thermophysics* **23**, 1115–1124 (2002).

³²J. Spiece, *Quantitative mapping of nanothermal transport via Scanning Thermal Microscopy* (Springer Nature, 2019).

³³M. Razeghi, J. Spiece, O. Oğuz, D. Pehlivanoğlu, Y. Huang, A. Sheraz, U. Başçı, P. S. Dobson, J. M. Weaver, P. Gehring, *et al.*, "Single-material mos2 thermoelectric junction enabled by substrate engineering," *npj 2D Materials and Applications* **7**, 36 (2023).

³⁴S. Gomès, N. Trannoy, and P. Grossel, "Dc thermal microscopy: study of the thermal exchange between a probe and a sample," *Measurement Science and Technology* **10**, 805 (1999).

³⁵K. Luo, Z. Shi, J. Varesi, and A. Majumdar, "Sensor nanofabrication, performance, and conduction mechanisms in scanning thermal microscopy," *Journal of Vacuum Science & Technology B: Microelectronics and Nanometer Structures Processing, Measurement, and Phenomena* **15**, 349–360 (1997).

³⁶Y. Zhang, W. Zhu, F. Hui, M. Lanza, T. Borca-Tasciuc, and M. Muñoz Rojo, "A review on principles and applications of scanning thermal microscopy (sthm)," *Advanced functional materials* **30**, 1900892 (2020).

³⁷A. Assy and S. Gomès, "Temperature-dependent capillary forces at nanocontacts for estimating the heat conduction through a water meniscus," *Nanotechnology* **26**, 355401 (2015).

³⁸M. M. Yovanovich, J. R. Culham, and P. Teertstra, "Analytical modeling of spreading resistance in flux tubes, half spaces, and compound disks," *IEEE Transactions on Components, Packaging, and Manufacturing Technology: Part A* **21**, 168–176 (2002).

³⁹Y. Muzychka, M. Sridhar, M. Yovanovich, and V. Antonetti, "Thermal spreading resistance in multilayered contacts: applications in thermal contact resistance," *Journal of thermophysics and heat transfer* **13**, 489–494 (1999).

⁴⁰M. M. Yovanovich, "Four decades of research on thermal contact, gap, and joint resistance in microelectronics," *IEEE transactions on components and packaging technologies* **28**, 182–206 (2005).

⁴¹Y. Muzychka, M. Yovanovich, and J. Culham, "Thermal spreading resistance in compound and orthotropic systems," *Journal of thermophysics and heat transfer* **18**, 45–51 (2004).

⁴²M. Yovanovich and E. Marotta, "Thermal spreading and contact," *Heat transfer handbook* **1**, 261 (2003).

⁴³D. P. Kennedy, "Spreading resistance in cylindrical semiconductor devices," *Journal of applied physics* **31**, 1490–1497 (1960).

⁴⁴Q. Zhang, W. Zhu, J. Zhou, and Y. Deng, "Realizing the accurate measurements of thermal conductivity over a wide range by scanning thermal microscopy combined with quantitative prediction of thermal contact resistance," *Small* **19**, 2300968 (2023).

⁴⁵S. Gomès, A. Assy, and P.-O. Chapuis, "Scanning thermal microscopy: A review," *physica status solidi (a)* **212**, 477–494 (2015).

⁴⁶M. Bahrami, J. R. Culham, M. M. Yovanovich, and G. E. Schneider, "Thermal contact resistance of nonconforming rough surfaces, part 2: thermal model," *Journal of Thermophysics and Heat Transfer* **18**, 218–227 (2004).

⁴⁷E. Puyoo, S. Grauby, J.-M. Rampnoux, E. Rouvière, and S. Dilhaire, "Thermal exchange radius measurement: Application to nanowire thermal imaging," *Review of Scientific Instruments* **81** (2010).

⁴⁸R. Stoner and H. Maris, "Kapitza conductance and heat flow between solids at temperatures from 50 to 300 k," *Physical Review B* **48**, 16373 (1993).

⁴⁹J. Lombard, F. Detcherry, and S. Merabia, "Influence of the electron-phonon interfacial conductance on the thermal transport at metal/dielectric interfaces," *Journal of Physics: Condensed Matter* **27**, 015007 (2014).

⁵⁰A. J. Schmidt, X. Chen, and G. Chen, "Pulse accumulation, radial heat conduction, and anisotropic thermal conductivity in pump-probe transient thermoreflectance," *Review of Scientific Instruments* **79** (2008).

⁵¹R. Cheaito, J. T. Gaskins, M. E. Caplan, B. F. Donovan, B. M. Foley, A. Giri, J. C. Duda, C. J. Szwejkowski, C. Constantin, H. J. Brown-Shaklee, *et al.*, "Thermal boundary conductance accumulation and interfacial phonon transmission: Measurements and theory," *Physical Review B* **91**, 035432 (2015).

⁵²P. E. Hopkins, J. R. Serrano, L. M. Phinney, S. P. Kearney, T. W. Grassner, and C. T. Harris, "Criteria for cross-plane dominated thermal transport in multilayer thin film systems during modulated laser heating," (2010).

⁵³H. Kwon, C. Perez, W. Park, M. Asheghi, and K. E. Goodson, "Thermal characterization of metal–oxide interfaces using time-domain thermoreflectance with nanograting transducers," *ACS Applied Materials & Interfaces* **13**, 58059–58065 (2021).

⁵⁴J. Zhu, D. Tang, W. Wang, J. Liu, K. W. Holub, and R. Yang, "Ultrafast thermoreflectance techniques for measuring thermal conductivity and interface thermal conductance of thin films," *Journal of Applied Physics* **108** (2010).

⁵⁵Y. Yang, A. Kushima, W. Han, H. Xin, and J. Li, "Liquid-like, self-healing aluminum oxide during deformation at room temperature," *Nano letters* **18**, 2492–2497 (2018).

⁵⁶J. Gorobez, B. Maack, and N. Nilius, "Growth of self-passivating oxide layers on aluminum—pressure and temperature dependence," *physica status solidi (b)* **258**, 2000559 (2021).

⁵⁷K. Fuchs, "The conductivity of thin metallic films according to the electron theory of metals," in *Mathematical Proceedings of the Cambridge Philosophical Society*, Vol. 34 (Cambridge University Press, 1938) pp. 100–108.

⁵⁸E. H. Sondheimer, "The mean free path of electrons in metals," *Advances in Physics* **1**, 1–42 (1952).

⁵⁹A. Jain and A. J. McGaughey, "Thermal transport by phonons and electrons in aluminum, silver, and gold from first principles," *Physical review B* **93**, 081206 (2016).

⁶⁰C. Kittel and P. McEuen, *Introduction to solid state physics* (John Wiley & Sons, 2018).

⁶¹J. Lugo and A. Oliva, "Thermal properties of metallic films at room conditions by the heating slope," *Journal of Thermophysics and Heat Transfer* **30**, 452–460 (2016).

⁶²L. S. Volkov, L. S. Palatnik, and A. T. Pugachev, "Investigation of the thermal properties of thin aluminum films," *Soviet Physics JETP* **43**, 1171–1174 (1976), translated from *Zhurnal Eksperimental'noi i Teoreticheskoi Fiziki*, Vol. 70, p. 2244 (1976).

⁶³Z. Wu, P. Kuo, W. Lanhua, S. Gu, and R. Thomas, "Photothermal characterization of optical thin films," *Thin Solid Films* **236**, 191–198 (1993).

⁶⁴J. S. Jin, J. S. Lee, and O. Kwon, "Electron effective mean free path and thermal conductivity predictions of metallic thin films," *Applied Physics Letters* **92**, 171910 (2008).

⁶⁵A. J. Schmidt, R. Cheaito, and M. Chiesa, "Characterization of thin metal films via frequency-domain thermoreflectance," *Journal of Applied Physics* **107**, 024908 (2010).

⁶⁶A. Mayadas and M. Shatzkes, "Electrical-resistivity model for polycrystalline films: the case of arbitrary reflection at external surfaces," *Physical review B* **1**, 1382 (1970).

⁶⁷D. Gall, "Electron mean free path in elemental metals," *Journal of Applied Physics* **119**, 085101 (2016).